Journal of Vacuum Science and Technology A

RESEARCH ARTICLE | JULY 01 2024

High growth rate metal organic chemical vapor deposition grown Ga_2O_3 (010) Schottky diodes

Special Collection: Gallium Oxide Materials and Devices

Sudipto Saha ; Lingyu Meng ; Dong Su Yu ; A. F. M. Anhar Uddin Bhuiyan ; Hongping Zhao ;
Uttam Singisetti

J. Vac. Sci. Technol. A 42, 042705 (2024)
https://doi.org/10.1116/6.0003533

JVST A
Journal of Vacuum Science & Technology A

ARTICLE

pubs.aip.org/avs/jv a

High growth rate metal organic chemical vapor deposition grown Ga_2O_3 (010) Schottky diodes

Cite as: J. Vac. Sci. Technol. A 42, 042705 (2024); doi: 10.1116/6.0003533
Submitted: 12 February 2024 · Accepted: 10 June 2024 ·
Published Online: 1 July 2024

Sudipto Saha,[1,a)] Lingyu Meng,[2] Dong Su Yu,[2] A. F. M. Anhar Uddin Bhuiyan,[2] Hongping Zhao,[2,3] and Uttam Singisetti[1]

AFFILIATIONS

[1]Electrical Engineering Department, University at Buffalo, Buffalo, New York 14260

[2]Department of Electrical and Computer Engineering, The Ohio State University, Columbus, Ohio 43210

[3]Department of Materials Science and Engineering, The Ohio State University, Columbus, Ohio 43210

Note: This paper is part of the Special Topic Collection on Gallium Oxide Materials and Devices. [a)]Author to whom correspondence should be addressed: sudiptos@buffalo.edu

ABSTRACT

We report on the growth of Si-doped homoepitaxial β-Ga_2O_3 thin films on (010) Ga_2O_3 substrates via metal-organic chemical vapor deposition (MOCVD) utilizing triethylgallium (TEGa) and trimethylgallium (TMGa) precursors. The epitaxial growth achieved an impressive 9.5 μm thickness at 3 μm/h using TMGa, a significant advance in material growth for electronic device fabrication. This paper systematically studies the Schottky barrier diodes fabricated on the three MOCVD-grown films, each exhibiting variations in the epilayer thickness, doping levels, and growth rates. The diode from the 2 μm thick Ga_2O_3 epilayer with TEGa precursor demonstrates promising forward current densities, the lowest specific on-resistance, and the lowest ideality factor, endorsing TEGa's potential for MOCVD growth. Conversely, the diode from the 9.5 μm thick Ga_2O_3 layer with TMGa precursor exhibits excellent characteristics in terms of lowest leakage current, highest on-off ratio, and highest reverse breakdown voltage of −510 V without any electric field management, emphasizing TMGa's suitability for achieving high growth rates in Ga_2O_3 epilayers for vertical power electronic devices.

I. INTRODUCTION

In recent years, there has been a growing interest in the development of ultrawide bandgap (UWBG) semiconductor materials for advanced power electronic applications.[1–6] This surge of interest is primarily driven by the potential for significantly higher switching efficiency and increased power conversion densities offered by UWBG semiconductors. Monoclinic beta-phase Ga_2O_3 (β-Ga_2O_3, hereafter referred to as Ga_2O_3) has gained substantial attention due to its exceptional characteristics, including a wide bandgap of ~4.8 eV, predicted breakdown field of ~8 MV/cm, and the unique advantage of cost-effective synthesis methods for free-standing native substrates.[7–11] Ga_2O_3's experimental field strengths also make it ideal for multikilovolt (>10 kV) devices suited for medium voltage grid applications. Furthermore, Ga_2O_3 stands out among UWBG materials due to its broad range of shallow n-type dopants and scalable, melt-grown native substrates that facilitate highquality homoepitaxy.[7,9–17] As a result, various high-performance Ga_2O_3 devices have been extensively studied, demonstrating impressive breakdown voltages and power device figures of merit.[18–23] Demonstrating superior capabilities, Ga_2O_3-based power devices suggest a potential to surpass those of traditional wide bandgap materials like silicon carbide (SiC) and gallium nitride (GaN), positioning Ga_2O_3 as a frontrunner for next-generation high-voltage power switching applications.[24,25]

However, vertical device configurations are increasingly adopted for most high-voltage and high-power applications by effectively mitigating surface effects and offering numerous advantages, including chip area scalability, higher current capability, improved field management, and enhanced thermal management.[25–33] Vertical Ga_2O_3 devices encounter significant performance challenges due to the absence of shallow p-type dopants. This scarcity is attributed to the large hole effective mass and the high ionization energy required for acceptors associated with conventional doping species in Ga_2O_3.[34–41] The absence of a p–n homojunction has led to the exploration of alternative rectifying junctions, such as Schottky barriers, p–n heterojunctions, and metal–insulator–semiconductor diodes.[42–45] Among these, the vertical n-type Schottky barrier diode (SBD) stands out as the primary rectifying device for Ga_2O_3 for its highquality interface.[45–48] Thin films of Ga_2O_3 have been grown on both native and foreign substrates using various techniques, including molecular beam epitaxy (MBE),[49,50] metal-organic chemical vapor deposition (MOCVD),[51–53] low-pressure chemical vapor deposition,[54,55] pulsed laser deposition,[56] and halide vapor phase epitaxy (HVPE).[57–60] MBE is characterized by a slow growth rate, attributed to the constrained evaporation from the metal source and desorption processes occurring under ultrahigh vacuum conditions, making the development of thick Ga_2O_3 drift layers using this technique impractical.[27,61] Thus far, HVPE has been favored for Ga_2O_3 vertical devices with thick drift layers, owing to its capability for fast growth rates of over 10 μm/h.[62,63] However, these HVPE-grown films with fast growth rates exhibit rough surface morphology with surface steps and pits,[58,64] necessitating expensive and potentially contaminating chemomechanical polishing before device manufacturing.[65] On the other hand, MOCVD is a promising technique that offers potential for high-quality Ga_2O_3 films, with a growth rate of ~1 μm/h, smooth surface morphology, controllable doping, and the highest room (~200 cm^2/V s) and low-temperature mobility (~10 000 cm^2/V s), as well as low compensating levels ($<10^{15}$ cm^{-3}), which directly affect power device performance, utilizing triethylgallium (TEGa) as the precursor.[66–70] The challenge, however, is to overcome an extremely slow growth rate. In contrast, trimethylgallium (TMGa) precursor in a close-coupled showerhead reactor, achieved a rapid growth rate of up to 9.8 μm/h,[71] although surface morphology and electrical transport characteristics were not thoroughly examined. Recent TMGa-based MOCVD reached 1.5 μm/h growth with promising surface quality (1.8 nm RMS).[70] This makes MOCVD a preferred growth method for Ga_2O_3 power devices. Although MOCVD growth of Ga_2O_3 using TMGa is relatively new and underexplored, a research gap exists concerning a comparative analysis of films grown with TEGa and TMGa, as well as the electrical properties of devices manufactured from these films. We present three MOCVD-grown Ga_2O_3 vertical SBDs fabricated on TEGa and TMGa-grown films.

This work investigated the MOCVD growth of Si-doped Ga_2O_3 homoepitaxial drift layers on (010) Sn-doped Ga_2O_3 substrates using TEGa and TMGa precursors. We conducted a comprehensive analysis of the surface morphology of the grown thin film using atomic force microscopy (AFM) and field emission scanning electron microscopy (FESEM). There are limited reports on the fabrication and characterization of vertical power devices' MOCVD-grown Ga_2O_3 films using different growth rates. The primary focus of this study is to explore an in-depth investigation into the electrical characteristics of three MOCVD-grown Ga_2O_3 Schottky diode samples, each differing in the epilayer thickness, doping levels, and growth rates. The promising Schottky diode characteristics in terms of the highest breakdown voltage, highest on-off ratios, and moderate field strength have been achieved from the highest reported Ga_2O_3 drift layer thickness grown using TMGa with a high growth rate (3 μm/h).

TABLE I. MOCVD growth conditions of Ga_2O_3 films on the Sn-doped (010) Ga_2O_3.

Sample ID	Estimated thickness[a] (μm)	TEGa/TMGa molar flow rate (μmol/min)	Growth temperature (°C)	Growth duration	Growth rate (μm/h)	Target electron concentration[b] (cm^{-3})

II. EXPERIMENT

Three Ga_2O_3 films were grown through MOCVD on Sn-doped (010) oriented Ga_2O_3 substrates (commercially acquired from Novel Crystal Technology, Inc.), labeled S1, S2, and S3. Prior to loading into the MOCVD growth chamber, Ga_2O_3 substrates were cleaned using acetone, isopropanol, and de-ionized water. High-purity oxygen (O_2) gas was used as the oxygen precursor, and argon (Ar) was the carrier gas. N-type doping was achieved using diluted silane (SiH_4) as the dopant source.

Sample S1 was grown under previously established conditions using trimethylgallium (TMGa) as the gallium precursor,[72] while samples S2 and S3 followed the growth conditions using triethylgallium (TEGa) as the gallium source.[69] The growth temperature for S1 (using TMGa) was maintained at 950 °C, whereas for S2 and S3 (using TEGa), it was set at 880 °C. All samples were grown at a constant pressure of 60 Torr. S1 achieved a thickness of 9.5 μm with a growth rate of 3 μm/h, while S2 and S3 reached thicknesses of 3 and 2 μm, respectively, with a growth rate of 0.65 μm/h. The targeted electron concentrations for S1, S2, and S3 were at 2×10^{16}, 2×10^{16}, and 7×10^{16} cm^{-3}, respectively. The electron concentrations in β-Ga_2O_3 were effectively controlled by tuning the silane molar flow rate during growth. Si acts as a shallow donor with a low activation energy in β-Ga_2O_3, making the electron concentration directly proportional to the silane molar flow rate, as demonstrated in previous studies.[69,72] These electron concentrations were also verified through room temperature Hall measurements conducted on the coloaded sample grown on Fe-doped (insulating) Ga_2O_3 substrates. Please refer to Table I in this study for a comprehensive overview of the growth conditions of the three Ga_2O_3 films grown on Sn-doped Ga_2O_3 substrates.

The surface morphologies of the β-Ga_2O_3 homoepitaxial thin films were characterized using FESEM (FEI Helios 650). Figures 1(a)–1(c) show the top view FESEM images of β-Ga_2O_3 homoepitaxial films grown on (010) Sn-doped β-Ga_2O_3 substrates. Despite S1 having the thickest film of 9.5 μm, S2 exhibits a higher

S1	9.5	TMGa, 58	950	3h	3	2–3 × 10^{16}
S2	3	TEGa, 31	880	4h 37 min	0.65	2 × 10^{16}
S3	2	TEGa, 31	880	3h 5min	0.65	7 × 10^{16}

[a] Estimated thickness is measured from SEM cross-sectional view of the coloaded c-sapphire samples.

[b] Estimated doping is from the Hall measurement of coloaded Fe-doped substrates.

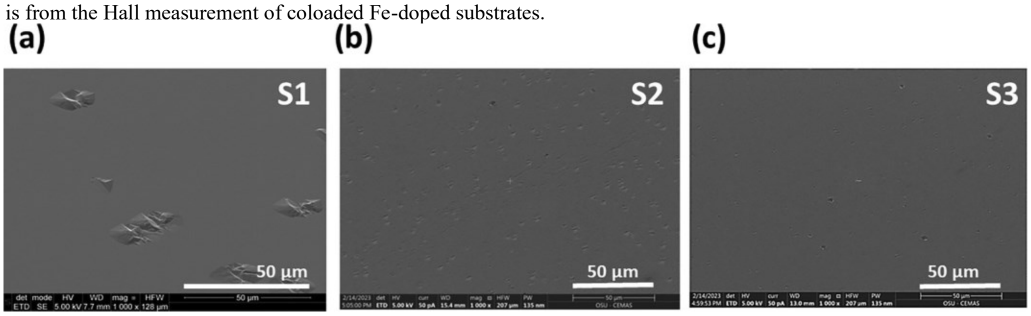

FIG. 1. FESEM images of MOCVD-grown β-Ga_2O_3 films on the (010) Sn-doped β-Ga_2O_3 substrate: (a) 9.5 µm (S1, TMGa); (b) 3 µm (S2, TEGa); and (c) 2 µm (S3, TEGa).

density of surface defects than S1. This increased defect density in S2 could be attributed to its longer growth duration, necessitated by the slower growth rate when using TEGa. In contrast, S3 demonstrates the smoothest surface due to its relatively thinner film thickness. The AFM analysis of the thin films revealed surface characteristics. Figures 2(a)–2(c) illustrate AFM images with a 5 × 5 µm^2 scan for all samples, where the RMS roughness values for S1, S2, and S3 thin films were 3.12, 11.4, and 10.7 nm, respectively. Despite S1 exhibiting lower micrometer-scale RMS roughness compared to other samples, it exhibits larger surface steps and pits on the macroscale. S1 has a lower pit density compared to S2 and S3, but the pits are notably large, likely due to its high growth rate. Conversely, although S2 and S3 have a higher pit density than S1, their pits are shallower, indicating a lower growth rate. S3, with a shorter growth duration, exhibits a smoother surface compared to S2.

Figure 3(a) illustrates a schematic cross section of the device structure employed for electrical testing. The fabrication process initiated with backside etching using BCl_3 reactive-ion etching, removing 1 µm thick Ga_2O_3. Subsequently, a Ti/Au Ohmic metal stack was deposited through electron beam evaporation and subjected to rapid thermal annealing in N_2 at 470 °C for 1 min Finally, the top Ni/Au Schottky contacts were defined by electron beam lithography. Following the fabrication of the devices, current density–voltage (J–V) measurements were performed at room temperature to extract the fundamental Schottky diode properties using the HP 4155B semiconductor parameter analyzer.

Furthermore, a standard reverse-biased capacitance–voltage (C–V) measurement on the Schottky contacts was performed using an Agilent 4294A precision impedance analyzer. A room temperature reverse breakdown measurement of the diodes was subsequently performed with the samples submerged in Fluorinert FC-40 dielectric liquid.

III. RESULTS AND DISCUSSION

As shown in Fig. 3(b), it is evident that all the samples exhibit rectifying behavior. In Fig. 3(c), plotted on a semilog scale, a linear current response is observed at low bias voltages ($V < 1$ V). However, at higher bias voltages ($V > 1$ V), the linearity deviates due to the presence of series resistance in all three samples. However, the turn-on behavior of device S1 is different from S2 and S3. This variation is likely due to the higher series resistance in S1, possibly

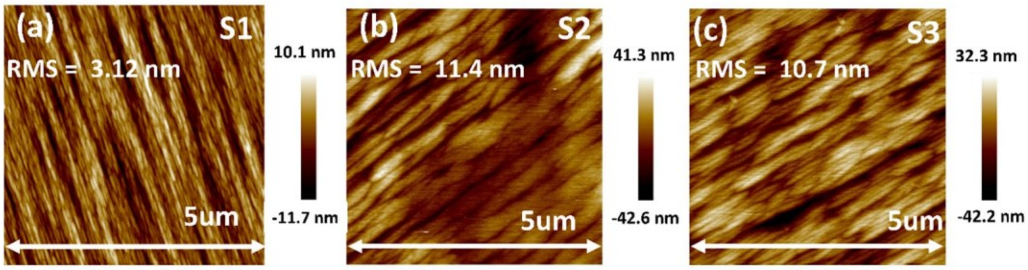

FIG. 2. 5 × 5 µm^2 area atomic force microscopy (AFM) scans of films before device fabrication: (a) 9.5 µm (S1, TMGa); (b) 3 µm (S2, TEGa); and (c) 2 µm (S3, TEGa).

resulting from surface roughness at the metalsemiconductor contact. Consequently, S1 exhibits a higher ideality factor (2.17 for S1) compared to the other two samples (1.73 for S2 and 1.31 for S3), indicative of its nonideal diode structure likely caused by the high parasitic resistance. The Schottky diodes were characterized to extract the fundamental Schottky diode properties using the current density–voltage (J–V) and capacitance–voltage (C–V) measurements at room temperature. Table II presents the extracted electrical properties. An ideality factor close to unity at room temperature implies nearly ideal Schottky behavior, where thermionic emission predominantly governs current transport.

The Schottky barrier height (SBH) can be measured from the following equation:

$$J_S \text{ ¼ } A^{*}T_2\, e^{\frac{q\Phi JV}{\eta(TB)kT}} : \qquad (1)$$

Here, J_S is the saturation current density, η is the ideality factor, T is the absolute temperature, q is the electron charge, k is the Boltzmann constant, $\Phi^{JV}{}_B$ is the apparent Schottky barrier height, A is the effective diode area, and A^* is the effective Richardson constant, calculated to be 41.04 A cm^{-2} T^{-2}.[73] The accuracy of Φ_B obtained from Eq. (2) depends on the corresponding value of the ideality factor. The measured Schottky barrier height from Eq. (1) is closer to the actual value if the ideality factor is close to 1, as described by Wagner et al.[74] As the ideality factor is >1 in our case, the corrected Schottky barrier height, Φ_B, is obtained using the following equation:

where N_C is the conduction density of states for Ga_2O_3 calculated using the electron effective mass of 0.34 m_0 with all other constants at their standard values.[75,76] N_D is the donor concentration of the Ga_2O_3.

As seen in Table II, there is a trend observed in ideality factors among the three Ga_2O_3 diode samples (S1, S2, and S3), which can be attributed to variations in surface quality and doping concentrations. The high ideality factor represents the prevalence of nonideal effects, notably the spatial inhomogeneity of Schottky barriers, likely arising from surface roughness at the metal–semiconductor interfaces. The diodes exhibit distinct characteristics, with S1 displaying the highest surface roughness on the macroscale and an ideality factor of 2.17, which suggests increased recombination centers associated with surface defects, possibly due to its macroscale roughness and highest growth rate. The higher η value in S1 indicates the presence of nonideal effects, including thermionic field emission, trap-assisted tunnel-

$$\Phi_B ¼ \Phi_B^{JV} \quad \frac{\eta \quad 1}{\eta}\frac{kT}{q}\ln\frac{N_C}{N_D} \quad \eta, \qquad (2)$$

ing currents, and the quality of metal adhesion and interfaces. In contrast, S2, characterized by a lower growth rate and thickness, demonstrates improved device quality, reflected in a lower ideality factor of 1.73. Notably, S3, distinguished by its smooth surface and a higher doping concentration of 7 × 10^{16} cm^{-3}, exhibits the most favorable performance with the lowest ideality factor of 1.31, suggesting enhanced carrier recombination characteristics. The

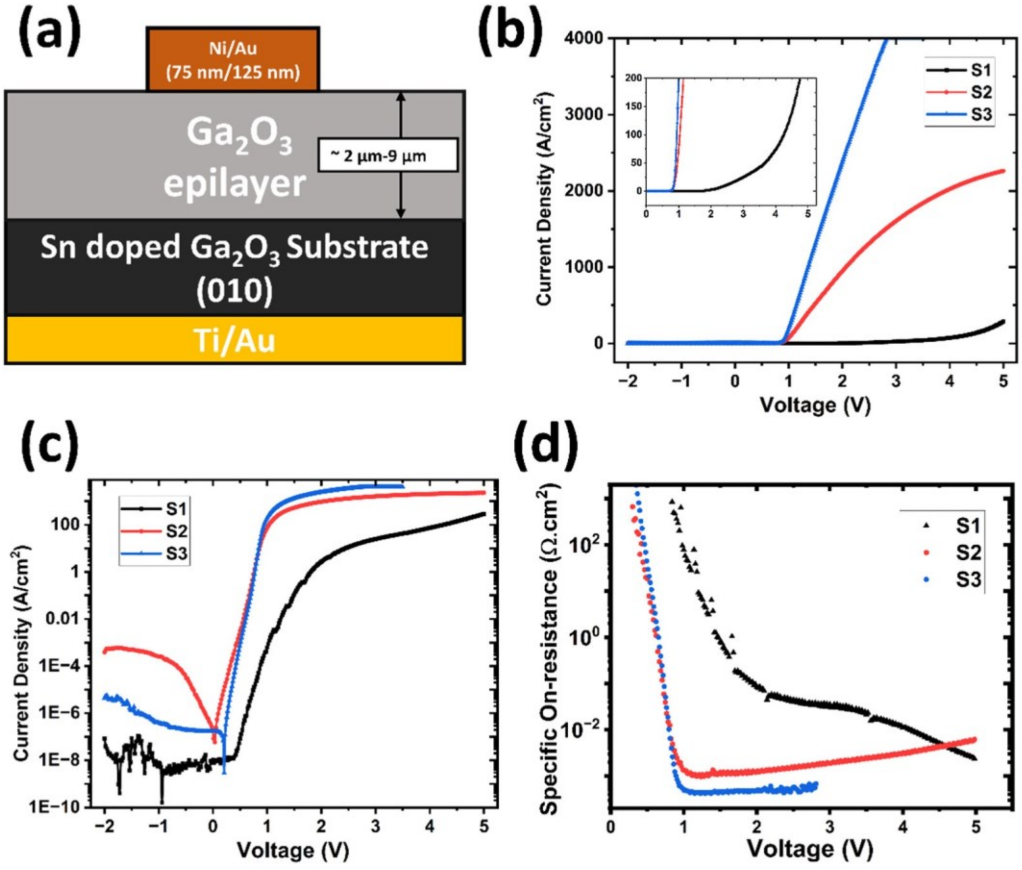

FIG. 3. (a) Schematic cross section of Ga_2O_3 vertical Schottky diode structures fabricated on (010) Ga_2O_3 substrates. (b) Room temperature forward current density (J) vs voltage (V) characteristics for S1, S2, and S3 Schottky barrier diodes. The inset shows forward characteristics of S1, S2, and S3. (c) Room temperature semilogarithmic current density (J) vs voltage (V) characteristics for S1, S2, and S3 Schottky barrier diodes. (d) Differential $R_{on,sp}$ for S1, S2, and S3 Schottky barrier diodes.

TABLE II. Extracted electrical properties at room temperature from J–V and C–V measurements for S1, S2, and S3.

		Derived from J–V			Derived from C–V	
Sample ID	Ideality factor, η	Barrier height, Φ_B (eV)	$R_{on,sp}$ (mΩ cm^{-2})	ON-OFF ratio	Barrier height, Φ_B (eV)	Average doping (cm^{-3})
S1	2.17	1.72	2.36	>10^9	3.13	2.02 × 10^{16}
S2	1.73	1.18	1.02	>10^7	1.80	2.82 × 10^{16}
S3	1.31	1.0	0.417	>10^8	1.66	6.08 × 10^{16}

measured Schottky barrier heights for S1, S2, and S3 from the J– V curve are 1.72, 1.18, and 1.0 eV, respectively. Thus, a smoother surface and higher doping concentration are observed to correlate with a reduced Schottky barrier height.[55] Therefore, S3, with the smoothest surface and the highest doping concentration, exhibits the lowest Schottky barrier height of 1.0 eV. S1, characterized by higher surface roughness and a lower doping concentration, shows the highest barrier height of 1.72 eV. S2, positioned between S1 and S3, demonstrates an intermediate barrier height of 1.18 eV. The calculated Schottky barrier heights agree with the values reported in the literature.[77–79] Nevertheless, the minimum differential specific on-resistance ($R_{on,sp}$) for the S1, S2, and S3 diodes have been extracted as 2.36, 1.02, and 0.417 mΩ cm^{-2}, respectively [Fig. 3(d)]. The S3 diode is the most favorable among the three samples. This can be attributed to the combination of a thinner epilayer, smoother surface, and higher doping concentration in S3. Among the examined four parameters— surface roughness, growth rate, epilayer thickness, and doping concentration—it appears that both epilayer thickness and doping concentration play pivotal roles in influencing specific on-resistance. Specifically, S1 (thicker epilayer, lower doping) demonstrates the highest $R_{on,sp}$ of 2.36 mΩ cm^{-2}. The slope of the J–V plot [Fig. 3(b)] for S2 begins to decrease beyond approximately 3 V, indicating an increase in the specific on-resistance for S2 after this voltage, as shown in Fig. 3(d).

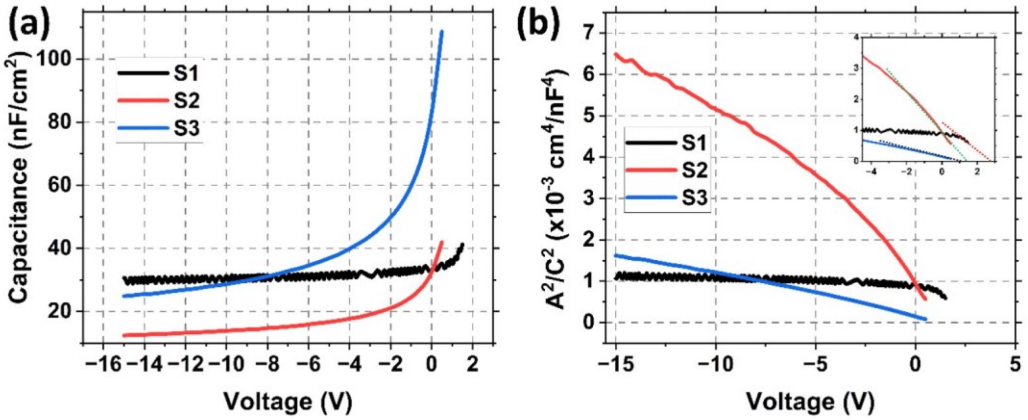

FIG. 4. (a) Capacitance (C) vs voltage (V) characteristics at room temperature and (b) $1/C^2$–V to extract V_{bi} for S1, S2, and S3 Schottky diodes.

Figure 4(a) shows the room temperature reverse bias C–V plots of the three samples, which indicated a complete depletion of the drift layers of the three samples. The 1 MHz C–V measurements revealed a net doping concentration of 2.02×10^{16}, 2.82×10^{16}, and 6.08×10^{16} cm^{-3} in the drift layers of the S1, S2, and S3 Schottky diodes, respectively (supplementary material).[82] These numbers match very well with the target electron concentrations mentioned in Table I. The S1 sample features a drift layer that is highly compensated, containing very few electrons (supplementary material).[82] The doping profile obtained from the CV plot exhibits high error bars. Therefore, the higher turn-on voltage and increased parasitic resistance may likely result from the combined impact of space charge limited transport and Schottky transport.

The $1/C^2$–V analysis, as seen in Fig. 4(b), also provided SBHs of S1, S2, and S3 diodes as 3.13, 1.80, and 1.66 eV, respectively, which were calculated from the extracted built-in voltage (V_{bi}) by accounting for the Fermi level position relative to the conduction band (E_C–E_F).[48,80] The barrier heights measured from the C–V characteristics of the samples are reasonable but slightly larger than the barrier heights measured from the J–V characteristics.

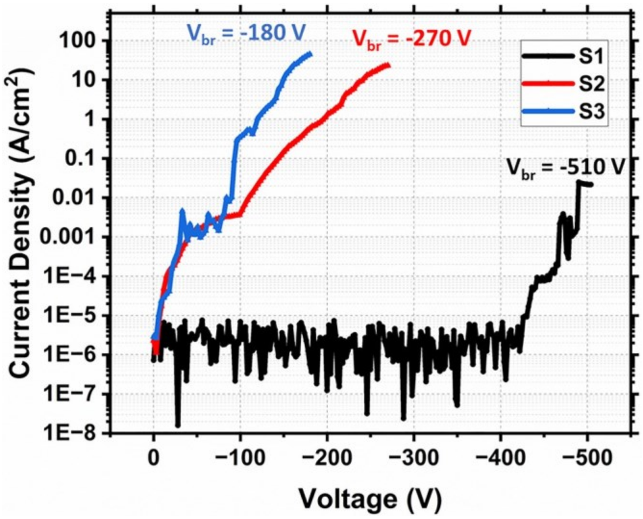

FIG. 5. Reverse J–V characteristics for S1, S2, and S3 Schottky barrier diodes. The device sizes are as follows: S1 is a square with a 50 µm side, and S2 and S3 are circles with a 35 µm radius.

However, both J–V and C–V measurements consistently exhibit that S1 has the highest SBH, while S3 has the lowest.

The reverse J–V characteristics of S1, S2, and S3 diodes are illustrated in Fig. 5. The destructive breakdown voltages are observed in the Schottky diodes as −510 V for S1, −270 V for S2, and −180 V for S3. Calculated field strengths correspondingly measure 0.54, 0.9, and 0.9 MV/cm for S1, S2, and S3, respectively. Differences in the drift layer thickness, doping concentrations, barrier heights, surface roughness, and overall device quality could influence the variation in the breakdown voltages of the three diode samples. Specifically, S1, with the thickest drift layer, exhibits a lower electric field strength and a higher breakdown voltage, while S3, with the thinnest layer, shows the opposite trend. S2 and S3 exhibit an identical calculated field strength of 0.9 MV/cm despite variations in breakdown voltage. This is likely due to the combination of a thinner drift layer and higher doping concentration in S2 and S3, leading to a more concentrated electric field. Surface roughness indirectly impacts semiconductor device breakdown voltage; improving smoothness, such as through chemical mechanical polishing, is anticipated to notably enhance reverse characteristics. However, the epilayer thickness, doping concentrations, and overall device quality are more direct determinants of the observed trend in destructive breakdown voltages. It is evident that the MOCVD-grown 9.5 µm thick Ga_2O_3 film (S1), achieved with the highest growth rate (3 µm/h) using TMGa, exhibits promising performance, in terms of the highest breakdown voltage, highest on-off ratios, and moderate field strength. The demonstrated potential of the high growth rate MOCVD technique to grow thick Ga_2O_3 drift layers underscores its promise for advancing high-voltage device applications. A comparative analysis of the MOCVD-grown Ga_2O_3 homoepitaxial thin films from this study as compared to data reported in the recent literature has been presented in Table III.

TABLE III. Comparative analysis of MOCVD-grown Ga_2O_3 homoepitaxial thin films from this study with recent literature data.

Report	Ga precursor	Growth rate (µm/h)	Epilayer thickness (µm)	Surface roughness, RMS (nm)	Reference
UCSB-Agnitron 2020	TEGa	1	3.2	0.8–16.4	66
Agnitron 2020	TMGa	1.5	2–5	∼1.8	70
UCSB 2024	TEGa	0.3–4.5	1.24–6.3	0.8–3.8	25
OSU 2022	TMGa	1.57–6.71	1.09–3.29	0.7–2.12	72
UMN-Agnitron 2023	TMGa	∼0.62–0.75	3.3–3.5	—	81
This work	TMGa	3	9.5	3.12	
This work	TEGa	0.65	2–3	∼11	

IV. CONCLUSIONS

In summary, three different Si-doped homoepitaxial Ga_2O_3 thin films were grown on Sn-doped (010) Ga_2O_3 substrates via MOCVD using both TEGa and TMGa as Ga precursors. The epitaxial growth of Ga_2O_3 material tailored for high-performance electronic devices is achieved with an impressive epilayer thickness of 9.5 µm, accomplished at a notably high growth rate of 3 µm/h using TMGa in an MOCVD reactor. This is a significant progress, surpassing prior reports in terms of both thickness and the growth rate in the context of electronic device-grade Ga_2O_3 material growth. Schottky diodes using the three MOCVD-grown films have also been demonstrated. The Schottky diode fabricated from the 2 µm thick Ga_2O_3 drift layer (S3) grown using TEGa precursor exhibits the highest forward current densities (4000 A/cm^2 at 3.5 V), lowest specific on-resistance (0.417 mΩ cm^{-2}), moderate On-off ratio ($>10^8$), and lowest ideality factor (1.31), indicating the promise of using TEGa as the gallium precursor for MOCVD growth for decent drift layer thicknesses. On the contrary, the Schottky diode fabricated from 9.5 µm thick Ga_2O_3 drift layer (S1), grown using TMGa precursor, shows the lowest leakage current (8.32×10^{-8} A/cm^2 at −2 V), highest on-off ratio ($>10^9$), and highest reverse breakdown voltage of −510 V without any electric field management, indicating the viability of using TMGa as gallium precursor for achieving high growth rate of Ga_2O_3 epilayer in MOCVD growth technique for vertical power electronic devices. The specific on-resistance of the samples also increases with the increasing growth rate. For all the samples, the average doping concentrations, measured from the C–V characteristics, match the target electron concentration. Overall, while MOCVD-grown thin films with TEGa, particularly at 2 and 3 µm, exhibit superior electrical performance concerning forward current density, on-off ratio, and specific on-resistance, TMGa-grown thick films at 9 µm also show promising electrical properties, especially in terms of breakdown voltage, reverse breakdown voltage, and on-off ratio. This establishes the viability of TMGa in thick film growth suitable for electronic devices in the MOCVD technique. The observed trends and characteristics in thick epilayer growth, especially at a high growth rate, position it as a valuable subject for further in-depth investigation and detailed exploration in Ga_2O_3 semiconductor device research. Achieving further advancements involves optimization of growth conditions to enhance surface smoothness. The findings underscore the potential of employing the MOCVD growth technique with a high growth rate for the deposition of thick Ga_2O_3 layers on native substrates. This holds significant promise, especially in developing vertical power devices, as this study demonstrated.

ACKNOWLEDGMENTS

We acknowledge the support from AFOSR (Air Force Office of Scientific Research) under Award No. FA9550-18-1-0479 (Program Manager: Ali Sayir), from National Science Foundation (NSF) under Award Nos. ECCS 2019749 and 2231026, and II–VI Foundation Block Gift Program. This work used the electron beam lithography system acquired through NSF MRI Award No. ECCS 1919798.

AUTHOR DECLARATIONS

Conflict of Interest

The authors have no conflicts to disclose.

Author Contributions

Sudipto Saha: Conceptualization (equal); Data curation (equal); Formal analysis (equal); Methodology (equal); Validation (equal); Writing – original draft (equal); Writing – review & editing (equal). **Lingyu Meng:** Data curation (equal); Formal analysis (equal); Validation (equal); Writing – original draft (supporting); Writing – review & editing (supporting). **Dong Su Yu:** Data curation (supporting); Formal analysis (supporting); Methodology (supporting); Validation (supporting); Writing – original draft (equal). **A. F. M. Anhar Uddin Bhuiyan:** Data curation (supporting); Formal analysis (supporting); Methodology (supporting). **Hongping Zhao:** Conceptualization (equal); Formal analysis (equal); Funding acquisition (equal); Investigation (equal); Methodology (equal); Resources (equal); Supervision (lead); Writing – original draft (equal). **Uttam Singisetti:** Conceptualization (equal); Formal analysis (equal); Funding acquisition (equal); Investigation (equal); Methodology (equal); Resources (equal); Supervision (equal); Writing – original draft (equal); Writing – review & editing (equal).

DATA AVAILABILITY

The data that support the findings of this study are available from the corresponding author upon reasonable request.

REFERENCES

[1] A. Q. Huang, Power Electronics in Renewable Energy Systems and Smart Grid (Wiley Online Library, 2019), pp. 85–152.

[2] H. Amano et al., J. Phys. D: Appl. Phys. 51, 163001 (2018).

[3] M. Higashiwaki, A. Kuramata, H. Murakami, and Y. Kumagai, J. Phys. D: Appl. Phys. 50, 333002 (2017).

[4] J. Y. Tsao et al., Adv. Electron. Mater. 4, 1600501 (2018).

[5] J. Yang, C. Fares, R. Elhassani, M. Xian, F. Ren, S. J. Pearton, M. Tadjer, and A. Kuramata, ECS J. Solid State Sci. Technol. 8, Q3159 (2019).

[6] Y. Zhang and T. Palacios, IEEE Trans. Electron. Devices 67, 3960 (2020).

[7] E. Farzana, F. Alema, W. Y. Ho, A. Mauze, T. Itoh, A. Osinsky, and J. S. Speck, Appl. Phys. Lett. 118, 162109 (2021).

[8] C. Joishi, S. Rafique, Z. Xia, L. Han, S. Krishnamoorthy, Y. Zhang, S. Lodha, H. Zhao, and S. Rajan, Appl. Phys. Express 11, 031101 (2018).

[9] W. Li et al., Appl. Phys. Lett. 113, 202101 (2018).

[10] Y. Yao, R. F. Davis, and L. M. Porter, J. Electron. Mater. 46, 2053 (2017).

[11] M. Higashiwaki, K. Sasaki, T. Kamimura, M. H. Wong, D. Krishnamurthy, A. Kuramata, T. Masui, and S. Yamakoshi, Appl. Phys. Lett. 103, 123511 (2013).

[12] M. Higashiwaki and G. H. Jessen, Appl. Phys. Lett. 112, 060401 (2018).

[13] T. Onuma, S. Saito, K. Sasaki, T. Masui, T. Yamaguchi, T. Honda, and M. Higashiwaki, Jpn. J. Appl. Phys. 54, 112601 (2015).

[14] E. G. Víllora, K. Shimamura, Y. Yoshikawa, K. Aoki, and N. Ichinose, J. Cryst. Growth 270, 420 (2004).

[15] A. Kuramata, K. Koshi, S. Watanabe, Y. Yamaoka, T. Masui, and S. Yamakoshi, Jpn. J. Appl. Phys. 55, 1202A2 (2016).

[16] H. Aida, K. Nishiguchi, H. Takeda, N. Aota, K. Sunakawa, and Y. Yaguchi, Jpn. J. Appl. Phys. 47, 8506 (2008).

[17] M. H. Wong, K. Sasaki, A. Kuramata, S. Yamakoshi, and M. Higashiwaki, IEEE Electron Device Lett. 37, 212 (2016).

[18] S. Sharma, K. Zeng, S. Saha, and U. Singisetti, IEEE Electron Device Lett. 41, 836 (2020).

[19] Y. Lv et al., IEEE Electron Device Lett. 41, 537 (2020).

[20] Y. Lv et al., IEEE Electron Device Lett. 40, 83 (2019).

[21] H. Zhou, K. Maize, G. Qiu, A. Shakouri, and P. D. Ye, Appl. Phys. Lett. 111, 092102 (2017).

[22] K. Zeng, A. Vaidya, and U. Singisetti, IEEE Electron Device Lett. 39, 1385 (2018).

[23]

J. K. Mun, K. Cho, W. Chang, H.-W. Jung, and J. Do, ECS J. Solid State Sci. Technol. 8, Q3079 (2019).

24 M. Higashiwaki, K. Sasaki, A. Kuramata, T. Masui, and S. Yamakoshi, Appl. Phys. Lett. 100, 013504 (2012).

25 A. Bhattacharyya, C. Peterson, K. Chanchaiworawit, S. Roy, Y. Liu, S. Rebollo, and S. Krishnamoorthy, Appl. Phys. Lett. 124, 010601 (2024).

26 S. Kumar, H. Murakami, Y. Kumagai, and M. Higashiwaki, Appl. Phys. Express 15, 054001 (2022).

27 K. Sasaki, A. Kuramata, T. Masui, E. G. Víllora, K. Shimamura, and S. Yamakoshi, Appl. Phys. Express 5, 035502 (2012).

28 N. Allen, M. Xiao, X. Yan, K. Sasaki, M. J. Tadjer, J. Ma, R. Zhang, H. Wang, and Y. Zhang, IEEE Electron Device Lett. 40, 1399 (2019).

29 P. H. Carey, J. Yang, F. Ren, R. Sharma, M. Law, and S. J. Pearton, ECS J. Solid State Sci. Technol. 8, Q3221 (2019).

30 S. Roy, A. Bhattacharyya, P. Ranga, H. Splawn, J. Leach, and S. Krishnamoorthy, IEEE Electron Device Lett. 42, 1140 (2021).

31 Z. A. Jian, S. Mohanty, and E. Ahmadi, Appl. Phys. Lett. 116, 152104 (2020).

32 F. Otsuka, H. Miyamoto, A. Takatsuka, S. Kunori, K. Sasaki, and A. Kuramata, Appl. Phys. Express 15, 016501 (2022).

33 M. H. Wong and M. Higashiwaki, IEEE Trans. Electron Devices 67, 3925 (2020).

34 H. Peelaers, J. L. Lyons, J. B. Varley, and C. G. Van de Walle, APL Mater. 7, 022519 (2019).

35 T. Gake, Y. Kumagai, and F. Oba, Phys. Rev. Mater. 3, 044603 (2019).

36 H. He, R. Orlando, M. A. Blanco, R. Pandey, E. Amzallag, I. Baraille, and M. Rérat, Phys. Rev. B 74, 195123 (2006).

37 A. Kyrtsos, M. Matsubara, and E. Bellotti, Appl. Phys. Lett. 112, 032108 (2018).

38 K. Yamaguchi, Solid State Commun. 131, 739 (2004).

39 J. L. Lyons, Semicond Sci. Technol. 33, 05LT02 (2018).

40 S. Saha, L. Meng, A. F. M. A. U. Bhuiyan, A. Sharma, C. N. Saha, H. Zhao, and U. Singisetti, Appl. Phys. Lett. 123, 132105 (2023).

41 R. Sharma, M. E. Law, F. Ren, A. Y. Polyakov, and S. J. Pearton, J. Vac. Sci. Technol. A 39, 060801 (2021).

42 W. Hao et al., Appl. Phys. Lett. 118, 043501 (2021).

43 Z. Xia et al., Appl. Phys. Lett. 115, 252104 (2019).

44 Z. Hu et al., IEEE Trans. Electron Devices 67, 5628 (2020).

45 W. Li, D. Saraswat, Y. Long, K. Nomoto, D. Jena, and H. G. Xing, Appl. Phys. Lett. 116, 192101 (2020).

46 D. Saraswat, W. Li, K. Nomoto, D. Jena, and H.G. Xing, in 2020 Device Research Conference (DRC) (IEEE, New York, 2020), pp. 1–2.

47 W. Li, D. Jena, and H. G. Xing, J. Appl. Phys. 131, 015702 (2022).

48 E. Farzana, A. Bhattacharyya, N. S. Hendricks, T. Itoh, S. Krishnamoorthy, and J. S. Speck, APL Mater. 10, 111104 (2022).

49 K. R. A. Sasaki, T. Nicoletti, L. M. Almeida, S. D. dos Santos, A. Nissimoff, M. Aoulaiche, E. Simoen, C. Claeys, and J. A. Martino, Solid State Electron. 97, 30 (2014).

50 H. Okumura, M. Kita, K. Sasaki, A. Kuramata, M. Higashiwaki, and J. S. Speck, Appl. Phys. Express 7, 095501 (2014).

51 N. M. Sbrockey, T. Salagaj, E. Coleman, G. S. Tompa, Y. Moon, and M. S. Kim, J. Electron. Mater. 44, 1357 (2015).

52 G. Wagner, M. Baldini, D. Gogova, M. Schmidbauer, R. Schewski, M. Albrecht, Z. Galazka, D. Klimm, and R. Fornari, Phys. Status Solidi A 211, 27 (2014).

53 F. Alema et al., Phys. Status Solidi A 214, 1600688 (2017).

54 S. Rafique, L. Han, A. T. Neal, S. Mou, M. J. Tadjer, R. H. French, and H. Zhao, Appl. Phys. Lett. 109, 132103 (2016).

55 S. Saha, L. Meng, Z. Feng, A. F. M. Anhar Uddin Bhuiyan, H. Zhao, and U. Singisetti, Appl. Phys. Lett. 120, 122106 (2022).

56 S. Müller, H. von Wenckstern, D. Splith, F. Schmidt, and M. Grundmann, Phys. Status Solidi A 211, 34 (2014).

57 K. Nomura, K. Goto, R. Togashi, H. Murakami, Y. Kumagai, A. Kuramata, S. Yamakoshi, and A. Koukitu, J. Cryst. Growth 405, 19 (2014).

58 H. Murakami et al., Appl. Phys. Express 8, 015503 (2015).

59 Y. Oshima, E. G. Víllora, and K. Shimamura, J. Cryst. Growth 410, 53 (2015).

60 V. I. Nikolaev, A. I. Pechnikov, S. I. Stepanov, I. P. Nikitina, A. N. Smirnov, A. V. Chikiryaka, S. S. Sharofidinov, V. E. Bougrov, and A. E. Romanov, Mater. Sci. Semicond. Process. 47, 16 (2016).

61 E. Ahmadi, O. S. Koksaldi, S. W. Kaun, Y. Oshima, D. B. Short, U. K. Mishra, and J. S. Speck, Appl. Phys. Express 10, 041102 (2017).

62 Z. Hu, K. Nomoto, W. Li, N. Tanen, K. Sasaki, A. Kuramata, T. Nakamura, D. Jena, and H. G. Xing, IEEE Electron Device Lett. 39, 869 (2018).

63 W. Li, K. Nomoto, Z. Hu, D. Jena, and H. G. Xing, IEEE Electron Device Lett. 41, 107 (2020).

64 J. H. Leach, K. Udwary, J. Rumsey, G. Dodson, H. Splawn, and K. R. Evans, APL Mater. 7, 022504 (2019).

65 K. Goto, K. Konishi, H. Murakami, Y. Kumagai, B. Monemar, M. Higashiwaki, A. Kuramata, and S. Yamakoshi, Thin Solid Films 666, 182 (2018).

66 F. Alema, Y. Zhang, A. Mauze, T. Itoh, J. S. Speck, B. Hertog, and A. Osinsky, AIP Adv. 10, 085002 (2020).

67 Z. Feng et al., Phys. Status Solidi RRL 14, 2000145 (2020).

68 F. Alema, Y. Zhang, A. Osinsky, N. Valente, A. Mauze, T. Itoh, and J. S. Speck, APL Mater. 7, 121110 (2019).

69 Z. Feng, A. F. M. Anhar Uddin Bhuiyan, M. R. Karim, and H. Zhao, Appl. Phys. Lett. 114, 250601 (2019).

70 G. Seryogin, F. Alema, N. Valente, H. Fu, E. Steinbrunner, A. T. Neal, S. Mou, A. Fine, and A. Osinsky, Appl. Phys. Lett. 117, 262101 (2020).

71 F. Alema, B. Hertog, A. Osinsky, P. Mukhopadhyay, M. Toporkov, and W. V. Schoenfeld, J. Cryst. Growth 475, 77 (2017).

72 L. Meng, Z. Feng, A. F. M. A. U. Bhuiyan, and H. Zhao, Cryst. Growth Des. 22, 3896 (2022).

73 A. Jayawardena, A. C. Ahyi, and S. Dhar, Semicond. Sci. Technol. 31, 115002 (2016).

74 L. F. Wagner, R. W. Young, and A. Sugerman, IEEE Electron Device Lett. 4, 320 (1983). 75

A. Vaidya et al., J. Appl. Phys. 126, 095702 (2019).

[76] I. Lee, A. Kumar, K. Zeng, U. Singisetti, and X. Yao, 2017 IEEE 5th Workshop on Wide Bandgap Power Devices and Applications (WiPDA) (IEEE, New York, 2017), pp. 185–189.

[77] Y. Yao, R. Gangireddy, J. Kim, K. K. Das, R. F. Davis, and L. M. Porter, J. Vac. Sci. Technol. B 35, 03D113 (2017).

[78] E. Farzana, Z. Zhang, P. K. Paul, A. R. Arehart, and S. A. Ringel, Appl. Phys. Lett. 110, 202102 (2017).

[79] S. Oh, G. Yang, and J. Kim, ECS J. Solid State Sci. Technol. 6, Q3022 (2017).

[80] E. Farzana, S. Roy, N. S. Hendricks, S. Krishnamoorthy, and J. S. Speck, Appl. Phys. Lett. 123, 192102 (2023).

[81] P. P. Sundaram, F. Liu, F. Alema, A. Osinsky, B. Jalan, and S. J. Koester, Appl. Phys. Lett. 122, 232105 (2023).

[82] See supplementary material online for the doping profile as a function of depth for S1, S2, and S3 samples. The room temperature J–V and C–V characteristics for S1 are also in the supplementary document.